PNAS RESEARCH ARTICLE | ENGINEERING

# Unveiling synergy of strain and ligand effects in metallic aerogel for electrocatalytic polyethylene terephthalate upcycling

Junliang Chen[a], Fangzhou Zhang[a], Min Kuang[a], Li Wang[a], Huaping Wang[a], Wei Li[b,1], and Jianping Yang[a,1]

Edited by Alexis Bell, University of California, Berkeley, CA; received October 27, 2023; accepted March 6, 2024

**Recently, there has been a notable surge in interest regarding reclaiming valuable chemicals from waste plastics. However, the energy-intensive conventional thermal catalysis does not align with the concept of sustainable development. Herein, we report a sustainable electrocatalytic approach allowing the selective synthesis of glycolic acid (GA) from waste polyethylene terephthalate (PET) over a $Pd_{67}Ag_{33}$ alloy catalyst under ambient conditions. Notably, $Pd_{67}Ag_{33}$ delivers a high mass activity of 9.7 A $mg_{Pd}^{-1}$ for ethylene glycol oxidation reaction (EGOR) and GA Faradaic efficiency of 92.7 %, representing the most active catalyst for selective GA synthesis. In situ experiments and computational simulations uncover that ligand effect induced by Ag incorporation enhances the GA selectivity by facilitating carbonyl intermediates desorption, while the lattice mismatch-triggered tensile strain optimizes the adsorption of *OH species to boost reaction kinetics. This work unveils the synergistic of strain and ligand effect in alloy catalyst and provides guidance for the design of future catalysts for PET upcycling. We further investigate the versatility of $Pd_{67}Ag_{33}$ catalyst on $CO_2$ reduction reaction ($CO_2$RR) and assemble EGOR//$CO_2$RR integrated electrolyzer, presenting a pioneering demonstration for reforming waste carbon resource (i.e., PET and $CO_2$) into high-value chemicals.**

electrocatalysis | PET upcycling | glycolic acid | ligand effect | tensile strain

## Significance

Electrochemical upcycling of polyethylene terephthalate holds significant promise for generating value-added chemicals and achieving carbon neutrality. Nevertheless, electrocatalytic ethylene glycol oxidation reaction involves multiple possible $C_1$ and $C_2$ pathways, resulting in complex potential products that requires additional processing paths for separation and purification. Here, we demonstrate that tuning the electronic and lattice structure of metallic aerogel catalyst is a powerful approach to simultaneously achieve the high activity and high glycolic acid selectivity. Our $Pd_{67}Ag_{33}$ catalyst exhibits outstanding performance over most of the state-of-the-art noble metal-based catalysts. This work not only provides insights into the structure–activity relationship at the molecule level but also presents innovative attempt for the construction of electrocatalytic waste carbonaceous coreforming system.

The exponential surge in plastic consumption, combined with inadequate waste management protocols, has raised substantial global concern regarding the issue of plastic waste. The accumulation of plastic waste in natural environments has already exceeded 6,300 million tons (Mt), with projections indicating a rise to approximately 12,000 Mt by 2050 (1). Polyethylene terephthalate (PET), extensively employed in packaging and textiles, exhibits an annual global production exceeding 70 Mt (2). However, a large proportion (>80%) of PET plastics end up in landfills and environment, rather than being recycled. Catalytic PET conversion presents a sustainable strategy for utilizing this carbon-rich resource, which not only produces valuable chemicals but also minimizes potential carbon emissions (3). Nevertheless, conventional thermal catalysis relying on the high temperature (~200 °C) and high pressure (>20 atm) results in significant energy consumption, which is not in line with the concept of environment-friendliness and sustainability (4–6). Hence, developing novel catalytic approaches allowing PET upcycling under milder conditions is of necessity (7–10).

Electrocatalytic PET upcycling, driven by renewable electricity, provides an attractive alternative to selectively oxidize PET-derived ethylene glycol (EG) into valuable chemicals under ambient conditions. It is pivotal to acknowledge that electrocatalytic ethylene glycol oxidation reaction (EGOR) involves multiple possible $C_1$ and $C_2$ pathways, thus resulting in complex potential products such as carbon dioxide ($CO_2$), formic acid (FA), glycolic acid (GA), and oxalic acid. Given GA is a high-value chemical and a cornerstone for degradable polyglycolic acid production (11), directing efforts toward conserving the C–C bond and fostering the selective formation of high-value GA from waste PET plastics is of paramount interest. Most recently, pioneers have discovered the potential to modulate the electron structure of active sites, thereby regulating catalyst-intermediate interactions to achieve the desired selective EG-to-GA conversion (12, 13). However, it remains a challenge to construct advanced catalysts to push the catalytic activity for GA synthesis to even higher levels. Pd-based materials have been recognized as the high active catalysts for thorough oxidation of EG into $CO_2$ in the fuel cell (14–18). Particularly intriguing is the integration of a second element (denoted as M) into Pd nanocrystals to form a PdM alloy phase, where the ligand and strain effects have been substantiated significance in tuning the interactions between catalyst and reactants, thus boosting the activity for EGOR in fuel cell (19–21). Despite its firmly entrenched reputation for exceptional activity in EGOR, the latent potential for the selective synthesis of high-value GA from EG on Pd-based alloy catalysts has been underestimated for a long time, leading to a noticeable research gap. Therefore, the prospect of tuning crystal and

Author contributions: W.L. and J.Y. designed research; J.C. performed research; W.L. contributed new reagents/analytic tools; F.Z., M.K., L.W., H.W., and J.Y. analyzed data; and J.C. wrote the paper.

The authors declare no competing interest.

This article is a PNAS Direct Submission.

Copyright © 2024 the Author(s). Published by PNAS. This article is distributed under Creative Commons Attribution-NonCommercial-NoDerivatives License 4.0 (CC BY-NC-ND).

[1]To whom correspondence may be addressed. Email: weilichem@fudan.edu.cn or jianpingyang@dhu.edu.cn.

This article contains supporting information online at https://www.pnas.org/lookup/suppl/doi:10.1073/pnas.2318853121/-/DCSupplemental.

Published April 17, 2024.

electronic configurations in Pd-based alloys and uncovering their effects on intermediate adsorption for the selective GA synthesis assumes paramount significance in steering the design of highly active and selective catalysts for electrocatalytic PET valorization.

In this work, we present a PdAg alloy aerogel as an electrochemical catalyst for the synthesis of GA from waste PET plastics. Remarkably, $Pd_{67}Ag_{33}$ not only delivers a high Faraday efficiency (FE) for GA of 92.7% at 1.0 V (vs. reversible hydrogen electrode, RHE) with high stability but also exhibits an excellent activity of 9.7 A $mg_{Pd}^{-1}$, 12.4 times higher than commercial 20% Pd/C. Evidently, it stands as the most potent catalyst for selective EG-to-GA conversion. Depth understanding of the structure–performance relationship on $Pd_{67}Ag_{33}$ in EGOR is acquired by operando Fourier transform infrared spectroscopy (FTIR) and density functional theory (DFT) calculations, which indicate the high activity and GA selectivity originates from the synergistic of strain and ligand effect: 1) the ligand effect triggered by electron transfer from Ag to Pd leads to the downshift of Pd's d-band center, which suppresses the excessive oxidation by means of facilitating the desorption of carbonyl intermediates; 2) the tensile strain can accelerate the adsorption of EG molecules and *OH species on catalyst, thus optimizes the EGOR kinetics. Additionally, the unique electron structure of $Pd_{67}Ag_{33}$ suppresses the poison of CO, thus favoring the electrochemical $CO_2$ reduction reaction ($CO_2$RR) with an impressive $FE_{FA}$ of 91.2% at −0.35 V. Notably, we employ $Pd_{67}Ag_{33}$ as a bifunctional catalyst for the coupling of EGOR and $CO_2$RR in an integrated electrolyzer and demonstrate >80% FE on both electrodes. In summary, this investigation not only provides invaluable perspectives on the pivotal roles played by the ligand effect and tensile strain in augmenting the selectivity and activity during the EG-to-GA conversion mediated by PdAg alloy catalysts but also presents a pioneering demonstration for reclaiming high-value chemicals from waste carbon resource via electrochemical covalorization of PET and $CO_2$.

## Results

**Material Synthesis and Characterization.** The PdAg hydrogel was synthesized via a two-step salting-out and cross-linking strategy (Fig. 1*A*). Briefly, the presence of trisodium citrate ions ($CA^-$) allows the formation of stable Pd and Ag colloidal solution, while the introduction of fluorine anions ($F^-$) disrupts the stability of colloidal solutions and facilitates the assembly of PdAg nanoparticles (NPs) that fuse into a cross-linked framework (22). The final PdAg aerogels were obtained via freeze drying (*SI Appendix*, Fig. S1). Transmission electron microscopy (TEM) images (Fig. 1*B*) visualized the cross-linked structure of $Pd_{67}Ag_{33}$, which was constituted by ultrathin nanowires interconnected with each other. The integrity of the cross-linked porous structure could be preserved across varying Pd/Ag ratios (*SI Appendix*, Fig. S2). The fused cross-linked pure Ag aerogel with a large diameter of about 42 nm was formed, signifying the occurrence of the fusion process in the case of Ag precursor exclusively. Simultaneously, an increase in nanowire diameters was noted with increasing concentrations of the Ag precursor, which could be ascribed to the structure-directing function of Ag during the nucleation and gelation of PdAg aerogels. Moreover, $N_2$ adsorption-desorption isotherms and the pore size distribution curves indicated a hierarchical structure with the coexistence of mesopores and macropores in aerogels (*SI Appendix*, Fig. S3). The $Pd_{67}Ag_{33}$ exhibited a large Brunauer–Emmett–Teller (BET) surface areas (89.8 $m^2/g$) and pore volumes (0.285 $cm^3\ g^{-1}$), which is conducive to exposure of the active sites and mass transfer. Particularly, with increasing Ag content, the specific surface area decreased, ranging from 144.8 $m^2/g$ for the pure Pd aerogel to 29.6 $m^2/g$ for the pure Ag aerogel (*SI Appendix*, Table S1). This phenomenon further underscored the structure-directing function of Ag on the porosity of the PdAg alloy aerogel, matching well with the TEM results.

The wide-angle powder X-ray diffraction (XRD) pattern (Fig. 1*C*) revealed a face-centered cubic (fcc) polycrystalline structure. The characteristic peak positioning between the corresponding peaks of pure Pd and pure Ag indicated the formation of bimetallic PdAg alloys (23). In contrast to pure Pd (prepared as a contrast catalyst), the reflections of PdAg alloy exhibited noticeable shifts toward lower 2θ values as the fraction of Ag increased (*SI Appendix*, Fig. S4), which suggested that doping Ag into Pd lattice could increase the lattice parameter and thus produce tensile strain. X-ray photoelectron spectroscopy (XPS) illustrated negative and positive shifts in Ag 3d doublet and Pd 3d doublet of $Pd_{67}Ag_{33}$, respectively, compared to the spectra of pristine Ag and Pd (Fig. 1 *D* and *E*) (24). Similar trends were observed in other PdAg alloys (*SI Appendix*, Fig. S5). These

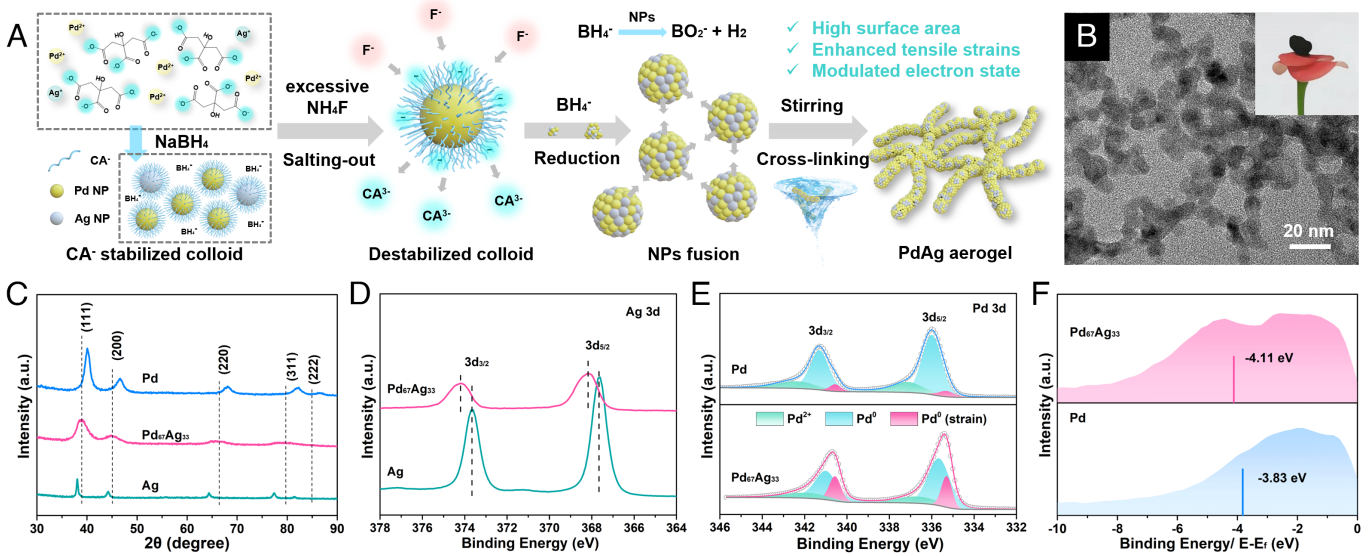


**Fig. 1.** Fabrication and characterization of $Pd_{67}Ag_{33}$ aerogel. (*A*) Schematic illustration of the preparation of PdAg aerogel. (*B*) TEM images (*Inset*: photograph) of $Pd_{67}Ag_{33}$ aerogel. (*C*) XRD patterns of $Pd_{67}Ag_{33}$ aerogel, pure Ag, and Pd aerogel. (*D*) High-resolution Ag 3d XPS spectra of $Pd_{67}Ag_{33}$ and pure Ag. (*E*) High-resolution Pd 3d XPS spectra of $Pd_{67}Ag_{33}$ and pure Pd. (*F*) Surface valence band photoemission spectra of $Pd_{67}Ag_{33}$ and pure Pd.

shifts indicated the electronic donation from Ag to Pd, which could be attributed to the higher working function of Pd (23). The increasing of $Pd^0$(strain)/$Pd^0$ area ratios further validated the abundant tensile strains in $Pd_{67}Ag_{33}$ (25), which is consistent with the XRD result. Furthermore, the surface valence band photoemission spectrum revealed a 0.28 eV downshift of the Pd d-band center in $Pd_{67}Ag_{33}$, which can be attributed to the increased electron filling of the Pd d-band resulting from the electron transfer from Ag to Pd (Fig. 1*F*). This downshift of the d-band center is expected to facilitate the desorption of carbonyl intermediates by weakening the binding strength on catalyst, which is essential to suppress the C–C bond cleavage and improve the selectivity toward $C_2$ products (12, 26).

Aberration-corrected high-angle annular dark-field scanning transmission electron microscopy (HAADF-STEM) image demonstrated the existence of abundant amorphous areas, defects, and boundaries (Fig. 2*A*). In contrast, Pd exhibited regularly arranged lattice fringes, indicating a lower presence of defects (*SI Appendix*, Fig. S6). As illustrated in Fig. 2*B*, the lattice spacings of 0.233, 0.210, and 0.196 nm correspond to the (111), (220), and (200) planes of $Pd_{67}Ag_{33}$ alloy, respectively (27). The fast Fourier transformation (FFT) pattern (*Inset* in Fig. 2*B*) further revealed the fcc polycrystalline structure. Elemental mapping images exhibited the evenly distribution of Pd and Ag elements with an atom ratio of 67.9:32.1 along the cross-linked nanowires (Fig. 2*C* and *SI Appendix*, Fig. S7). Similar atom Pd/Ag ratio of $Pd_{67}Ag_{33}$ (i.e., 68.3/31.7 and 65.2/34.8) was characterized by the inductively coupled plasma optical emission spectroscopy (ICP-OES) and XPS result (*SI Appendix*, Tables S2 and S3). As shown in Fig. 2 *D* and *E*, the lattice spacing corresponding to (111) crystal plane of Pd gauged in HRTEM is 2.244 Å, while the value detected by $Pd_{67}Ag_{33}$ in the identical region is 2.328 Å, indicating the introduction of tensile strain in $Pd_{67}Ag_{33}$ by alloying Ag into Pd lattice. Consequently, an approximate 3.7% lattice expansion (3.7% tensile strain) in the (111) lattice plane of $Pd_{67}Ag_{33}$ was occurred compared with pure Pd (Fig. 2*F*). Furthermore, we measured the specific lattice strain distribution by geometric phase analysis (GPA) to identify the strain distribution of $Pd_{67}Ag_{33}$. The strain mapping was obtained from the abreaction-corrected HAADF-STEM results after FFT and inverse FFT, significant chromatic aberration changes indicated a tensile strain–dominated structure (Fig. 2 *G*–*I*).

**Selective Electrochemical EG-to-GA Conversion Over $Pd_{67}Ag_{33}$.** Electrocatalytic activity and selectivity of the pure Pd and PdAg aerogels toward EGOR were evaluated in a standard three-electrode system. The linear sweep voltammetry (LSV) curves obtained from the pure Pd and $Pd_{67}Ag_{33}$ aerogel in a $N_2$-saturated 1 M KOH solution with and without 1 M EG at a scan rate of 10 mV $s^{-1}$. For

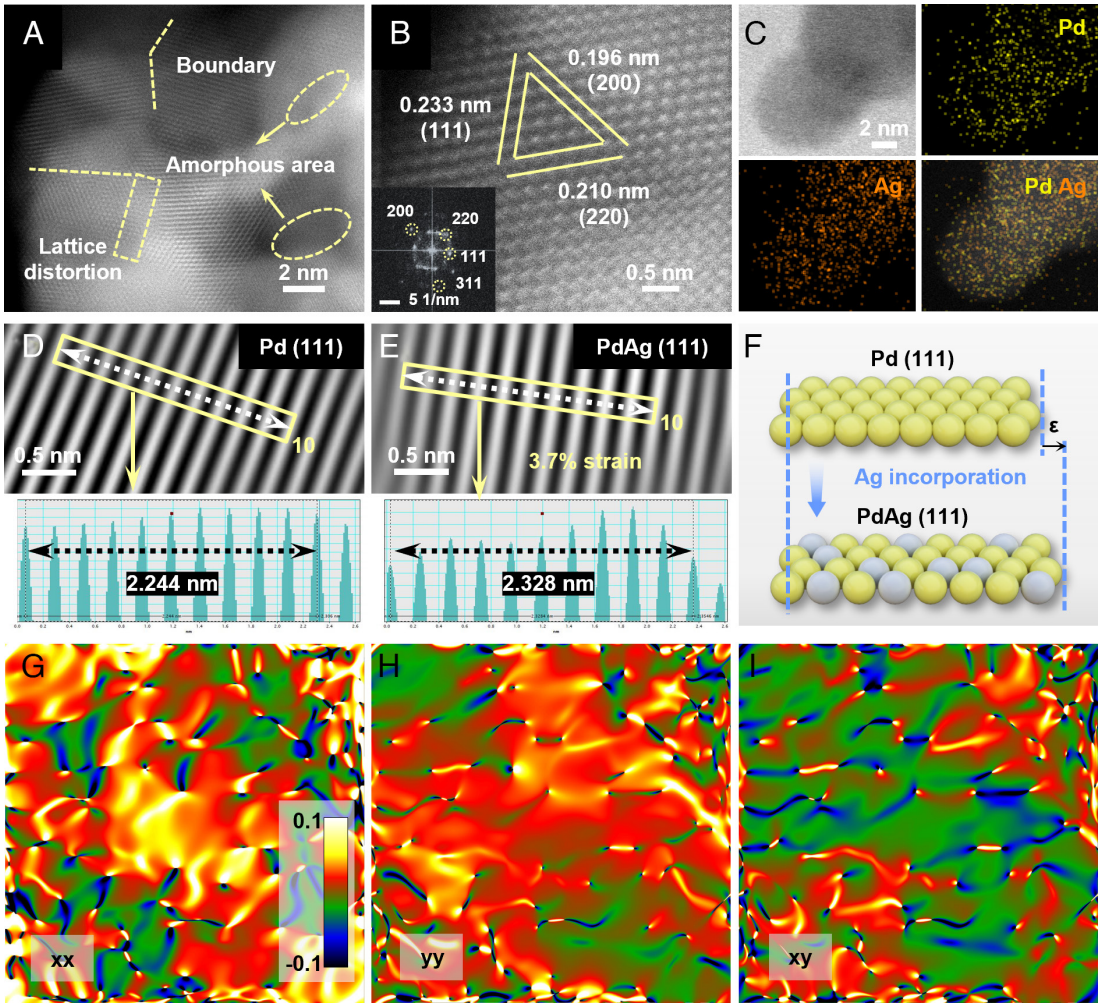


**Fig. 2.** Aberration-corrected HAADF-STEM images of $Pd_{67}Ag_{33}$ aerogel. (*A*) TEM image and (*B*) high-resolution TEM image and the corresponding FFT pattern of $Pd_{67}Ag_{33}$ aerogel. (*C*) HAADF-STEM and the corresponding elemental mapping images of $Pd_{67}Ag_{33}$ aerogel. (*D* and *E*) Inverse IFFT images of Pd and $Pd_{67}Ag_{33}$, the *Insets* correspond to the lattice spacing distribution. (*F*) Illustration for the lattice expansion of Pd and $Pd_{67}Ag_{33}$. (*G*–*I*) Maps of the in-plan strain tensors xx, yy, xy, processed via GPA (the color regions ranging from green to dark blue denote the compressive strain, while the regions from red to bright yellow represent the tensile strain).

comparison, a lower applied anodic potential of 0.53 V (vs. RHE) was required by $Pd_{67}Ag_{33}$ aerogel to reach 10 mA $cm^{-2}$ in the presence of 1 M EG (Fig. 3*A*). The significant reduction in overpotential (1,080 mV) suggested the thermodynamically favorable feature of EGOR compared to OER. Meanwhile, the comparation of LSV curves and Tafel slope plots between $Pd_{67}Ag_{33}$ and Pd indicated the boosted oxidation kinetics on $Pd_{67}Ag_{33}$, attributed to the fine modulation in electron and lattice structure (Fig. 3*B*). Cyclic voltammetry CV curves displayed a significantly lower onset potential of $Pd_{67}Ag_{33}$, implying the optimized adsorption and activation of EG molecules on $Pd_{67}Ag_{33}$ (Fig. 3*C*). Notably, $Pd_{67}Ag_{33}$ delivered exceptional mass activity of 9.7 A $mg_{Pd}^{-1}$, 3.2 and 12.4 times more than that of Pd aerogel catalyst (3.0 A $mg_{Pd}^{-1}$) and commercial 20 % Pd/C (0.8 A $mg_{Pd}^{-1}$) (*SI Appendix*, Figs. S8–S11). Furthermore, the comparison of the forward current density ($I_f$) and the backward current density ($I_b$) of catalysts illustrated higher $I_f/I_b$ values of $Pd_{67}Ag_{33}$, suggesting the Ag incorporation allows superior poisoning tolerance regarding the intermediate carbonaceous species in EGOR (*SI Appendix*, Fig. S12) (28). Electrochemical impedance spectroscopy (EIS) displayed lower electron transfer resistance ($R_{ct}$) of $Pd_{67}Ag_{33}$, suggesting the enhanced electron transfer kinetics in catalytic reactions (*SI Appendix*, Fig. S13). The electrochemical active surface areas (ECSAs) of samples were evaluated by the double-layer capacitance ($C_{dl}$), which implied more exposed active sites on $Pd_{67}Ag_{33}$ (*SI Appendix*, Fig. S14) (29). These active sites potentially originated from the defect-rich and amorphous structure, which endows $Pd_{67}Ag_{33}$ with the enriched coordination unsaturated surface sites, thereby facilitating the engagement in performance of EGOR (30, 31). Moreover, the catalytic activities in EGOR over the $Pd_xAg_y$ (y = 13 to 67%) alloy aerogels were further investigated (*SI Appendix*, Fig. S15). The mass activities exhibited a distinctive volcanic trend with increasing Ag content, initially ascending and subsequently descending. As mentioned above, the incorporation of Ag into Pd lattice structure triggered tensile strains and ligand effect, thereby promoting the adsorption of *OH species and the desorption of *CO species (12, 25). Thus, the enhanced EG adsorption and boosted intermediate conversion occurred on the surface of catalyst, which both contributed to heightened the catalytic activity. The CV curve of Ag aerogel indicated the inferior intrinsic catalytic activity of Ag for EGOR, with the mass activity of Ag observed to be two orders of magnitude lower than that of Pd (*SI Appendix*, Fig. S16). This result further revealed that the activity improvement of PdAg catalysts originated from the synergy of ligand and strain effects by Ag incorporation. However,

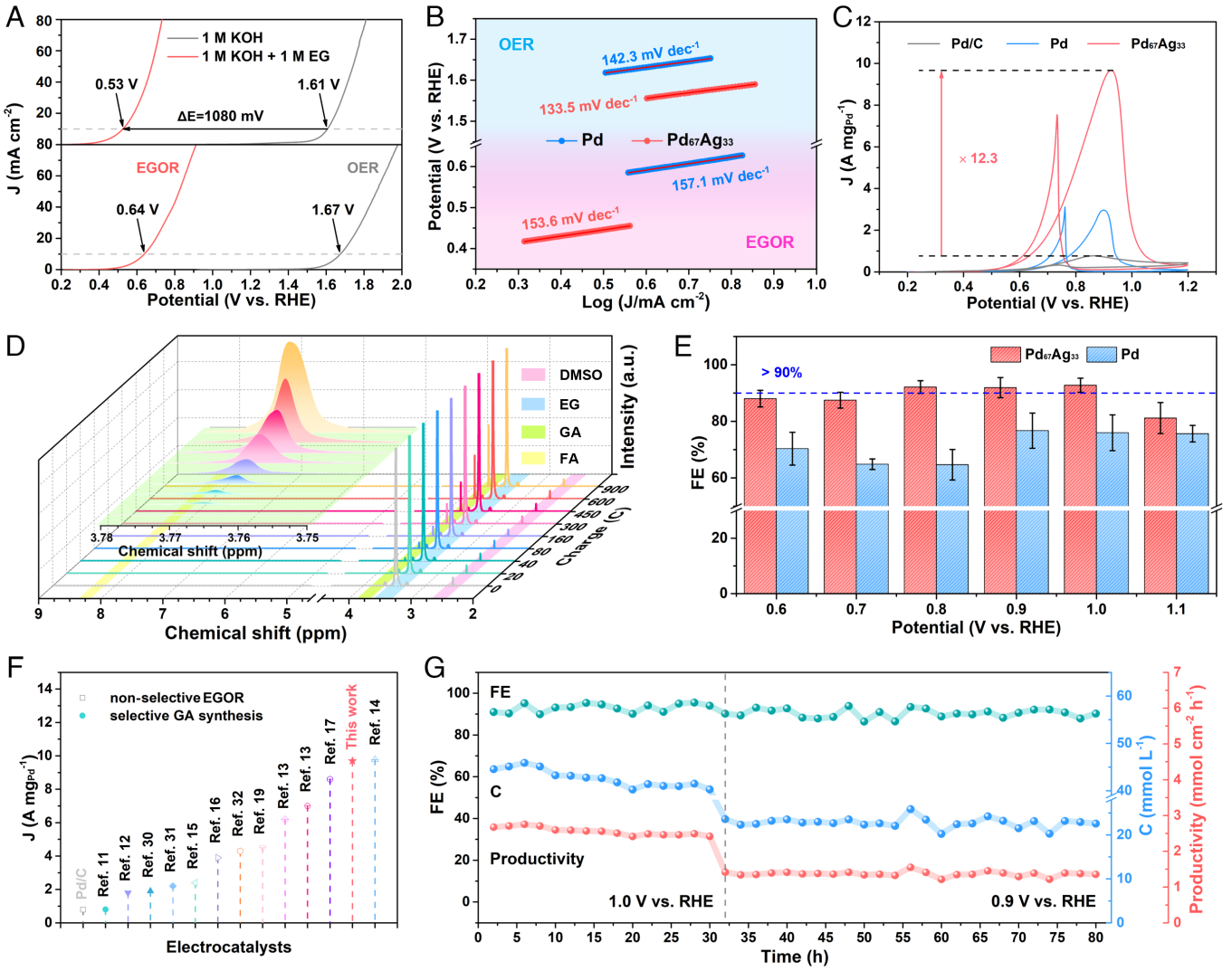


**Fig. 3.** Electrocatalytic performance of $Pd_{67}Ag_{33}$ aerogel toward anodic EGOR. (*A*) LSV curves, (*B*) Tafel slope plots, and (*C*) CV curves of Pd and $Pd_{67}Ag_{33}$ catalyst in 1 M KOH/1 M EG. (*D*) $^1$H NMR spectra of electrolyte with different charges passed at the applied potential of 1.0 V. (*E*) Potential dependence of FE for GA production on Pd and $Pd_{67}Ag_{33}$. (*F*) Comparison of mass activity for various EGOR catalysts reported previously, where the hollow symbols denote as the nonselective catalysts, while the solid symbols denote as the catalysts for selective GA synthesis. (*G*) 80-h stability test of $Pd_{67}Ag_{33}$ toward GA production.

as the Ag fraction reached an elevated level, the catalysts may lose active surface Pd sites along the nanochain structure, thus impeding reactant adsorption and conversion. Meanwhile, an increased Ag fraction enlarges the sizes of assembly unit of aerogels, resulting in reduced specific surface area that hampers mass transfer processes, leading to unfavorable kinetics for EGOR (32). Consequently, the $Pd_{67}Ag_{33}$ possessing a moderate fraction of Ag delivered an optimal activity.

To identify the product selectivity of the EG-to-GA conversion, $^{1}H$ and $^{13}C$ NMR spectroscopy was conducted. As shown in Fig. 3*D*, the evolution of peak of GA (~3.77 ppm, green shadow) at different charge passed demonstrated the dynamic EG-to-GA conversion on $Pd_{67}Ag_{33}$. Meanwhile, neither FA (~8.3 ppm, green shadow) nor other potential EGOR products could be found during electrolysis, indicating the circumvention of C–C bond cleavage and the selective GA production. $^{13}C$ NMR spectrum also exhibited the same result, further verifying the selective synthesis of GA on $Pd_{67}Ag_{33}$ (*SI Appendix*, Fig. S17). The quantitative analysis of the Faradic efficiencies toward GA was carried out at different applied potentials (Fig. 3*E* and *SI Appendix*, Fig. S18). At the potential of 1.0 V vs. RHE, a maximum $FE_{GA}$ of 92.7% was rendered over the $Pd_{67}Ag_{33}$, which is much higher than that of pure Pd and is of advantage among previous catalysts for EG-to-GA conversion. The concentration variation of EG and GA within 600 C charge implied the linear correlation between the consumption of EG and the production of GA during electrolysis (*SI Appendix*, Fig. S19). The $FE_{GA}$ of as-synthesized $Pd_xAg_y$ aerogels with different Pd/Ag ratios were also evaluated to investigate the influence of Ag addition on EG-to-GA conversion (*SI Appendix*, Fig. S20). Volcanic trends of $FE_{GA}$ with increasing Ag content were illustrated, presenting the $Pd_{67}Ag_{33}$ as the most selective catalyst for GA synthesis (*SI Appendix*, Fig. S21). As previous works reported, although the introduction of Ag could downshift the d-band center of Pd to preserve the C–C bond, substantial Ag incorporated into Pd lattice triggered high tensile strain contributes to upshift the d-band center (33, 34). Therefore, highly strained $Pd_xAg_y$ catalyst could enhance the surface binding strength toward *CO intermediate, thus facilitating the C–C bond cleavage and decreasing the GA selectivity (18, 25). This finding revealed the trade-off of strain effect in PdAg alloy catalysts to optimize the selective EG-to-GA conversion. To the best of our knowledge, the $Pd_{67}Ag_{33}$ represented the best active electrocatalysts for selective GA synthesis in EGOR to date (Fig. 3*F* and *SI Appendix*, Tables S5 and S6) (12–18, 20, 35–37), where the mass activity of 9.7 A $mg_{Pd}^{-1}$ is much higher than that of other catalysts (0.8 to 2.2 A $mg_{Pd}^{-1}$) for EG-to-GA conversion. Stability of catalysts was evaluated through a chronoamperometric method. The chronoamperometric curve of $Pd_{67}Ag_{33}$ displayed a dramatically improved durability of an 83.8 % retention of current density after 2 h measurement, which is much higher than that of Pd (24.4%) (*SI Appendix*, Figs. S22 and S23), aligning with the superior antipoisoning ability predicted by the higher $I_f/I_b$ values (*SI Appendix*, Fig. S12). During the 80-h-cyclic chronoamperometric tests, the initial current of $Pd_{67}Ag_{33}$ could be recovered as the electrolyte was refreshed (*SI Appendix*, Fig. S24). As illustrated in Fig. 3*G*, the average GA selectivity of 91.4% and GA productivity of 2.56 mmol $cm^{-2}$ $h^{-1}$ could be well preserved on $Pd_{67}Ag_{33}$, indicating excellent stability in the long-term electrocatalysis. XRD, XPS, and TEM measurements further verified the excellent durability of $Pd_{67}Ag_{33}$ catalyst with respect to structure and composition after long-term electrolysis (*SI Appendix*, Figs. S25–S27). To align PET upcycling with practical applications, our endeavor involved the valorization of real-word drink bottles via base catalysis depolymerization followed by electrocatalytic upcycling (*SI Appendix*, Fig. S28). First, terephthalate (TPA-K) and EG constituent monomers were obtained via the hydrolysis of PET bottles in 3 M KOH. Subsequently, EG monomer was utilized as a feedstock for further electrochemical valorization into glycollate. Following this, high-purity GA products can be obtained from the electrolyte by a series of separation and purification processes. XRD characterization, $^{13}C$ and $^{1}H$ NMR spectroscopy demonstrated the high purity of collected GA and TPA powders (*SI Appendix*, Figs. S29 and S30). Finally, 10 g of PET feedstock gave 8.26 g TPA (yield: 95.5%), 2.28 g GA (yield: 57.4%), demonstrating the readiness of this technique for practical applications.

**Insight of the Selective Adsorption and Conversion of Intermediates on Catalysts.** To give in-depth understanding of the structure–performance relationship for the EG-to-GA conversion over $Pd_{67}Ag_{33}$, in situ electrochemical measurements, radical probe tests, and quenching experiments were employed. First, we evaluated the EG adsorption on catalysts by the open-circuit potential (OCP) test. By adding 0.1 M EG into the electrooxidation system, the most marked decrease in OCP over $Pd_{67}Ag_{33}$ electrode illustrated the optimized EG adsorption (*SI Appendix*, Fig. S31). The adsorption behavior of $^{-}OH$ species on catalysts was investigated by CV measurements in 1 M KOH electrolyte. As illustrated in Fig. 4*A*, stronger Pd oxidation peaks (0.9 to 1.2 V) and PdO reduction peaks (0.5 to 0.9 V) of $Pd_{67}Ag_{33}$ suggested the sufficient defects and boundaries supplying more available active sites to participate the EGOR (38). The observed negative shift of the $^{-}OH$ adsorption peak indicated an optimized $^{-}OH$ adsorption process on $Pd_{67}Ag_{33}$, suggesting the alloying strategy could enhance the affinity of $^{-}OH$ on catalyst. Meanwhile, the CV curve of $Pd_{67}Ag_{33}$ displayed a negative shifted reduction peak of Pd along with higher intensity, signifying an increased binding energy of *OH adspecies ($*OH_{ad}$). To further identify the $*OH_{ad}$ on catalysts, electron paramagnetic resonance (EPR) experiment was carried out with the presence of 5,5-dimethyl-1-pyrroline N-oxide (DMPO) as spin trapping agents. A strong typical four-line characteristic DMPO–$^{\cdot}OH$ signals with an intensity ratio of 1:2:2:1 was detected in the $Pd_{67}Ag_{33}$/KOH system, implying the accelerated $^{\cdot}OH$ evolution upon $Pd_{67}Ag_{33}$ (Fig. 4*B*). As the injection of EG, new signal peaks identified as alkoxy radicals (DMPO–$^{\cdot}OR$) were detected and the DMPO–$^{\cdot}OH$ signals were slightly weakened, implying that $*OH_{ad}$ played a vital role in converting EG into $^{\cdot}OR$ (Fig. 4*C*). Furthermore, the productivity of $*OH_{ad}$ over catalysts were quantified by fluorescence probe experiments using coumarin as a fluorescence probe, where the higher fluorescence intensity in $Pd_{67}Ag_{33}$/KOH system suggested the superior $*OH_{ad}$ productivity (Fig. 4*D*) (39). In comparison with the $Pd_{67}Ag_{33}$/KOH system, the $Pd_{67}Ag_{33}$/KOH/EG system displayed a decreased fluorescence intensity (*SI Appendix*, Fig. S32), which corroborates with the result that *OH serves as an active species for EGOR.

We further employed Cu as a substitute for Ag to alloy with Pd to uncover the pivotal role of tensile strain in accelerating the kinetics for EGOR. The substitution of Cu in the Pd lattice structure induces compressive strain due to its smaller atomic radius than Pd (40, 41). Accordingly, we prepared a $Pd_{67}Cu_{33}$ alloy aerogel catalyst using the same salting-out and cross-linking method to investigate the structure–performance relationship. Both XRD pattern and HR-TEM image of $Pd_{67}Cu_{33}$ revealed a reduction in lattice spacing of the (111) crystal plane, confirming the successful fabrication of compressive strained $Pd_{67}Cu_{33}$ (*SI Appendix*,

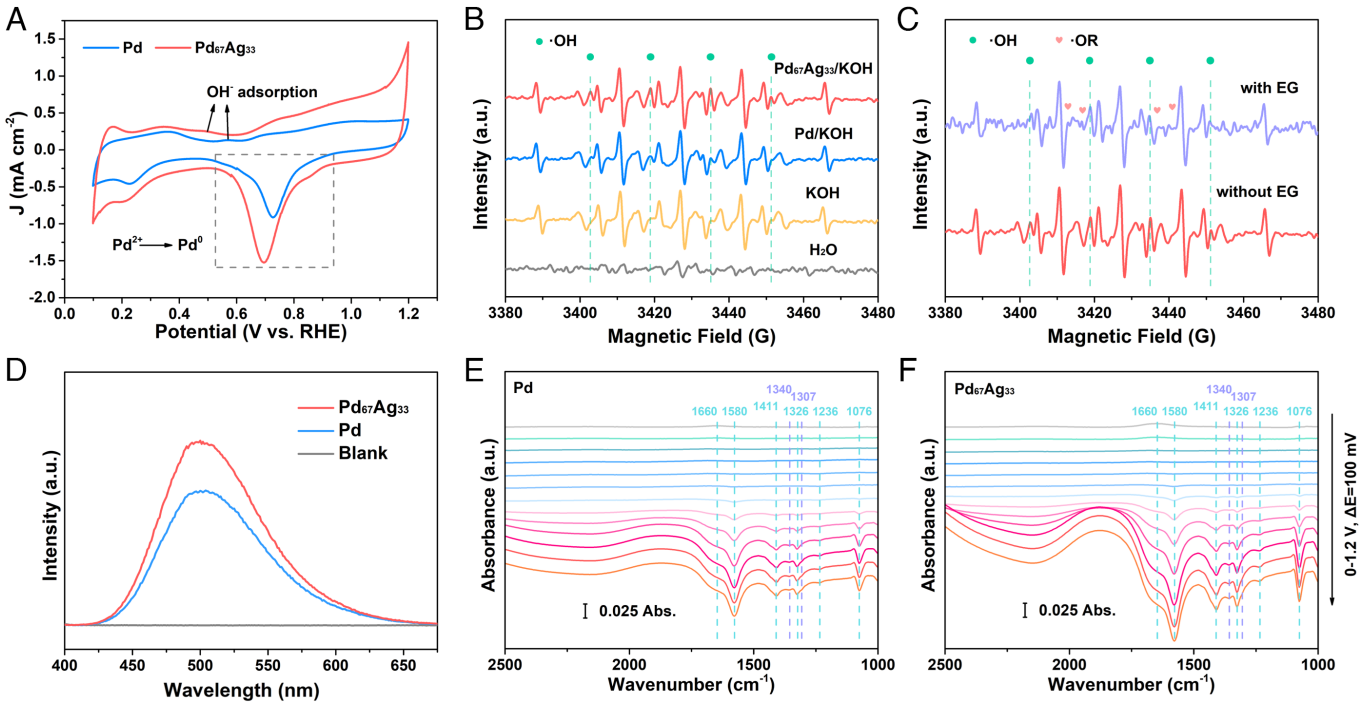


**Fig. 4.** Insight of the selective adsorption and conversion of intermediates on catalysts. (*A*) CV curves of Pd and $Pd_{67}Ag_{33}$ aerogel in 1 M KOH. (*B* and *C*) EPR spectra from the electrolyte using DMPO as a trapping agent: (*B*) OER and (*C*) EGOR. (*D*) Fluorescence spectra for the detected $^{-}$OH radicals in electrolyte using a coumarin (0.2 mM) indicator. (*E* and *F*) In situ electrochemical FTIR spectra under EGOR operation on Pd and $Pd_{67}Ag_{33}$.

Fig. S33). XPS spectra depicted the electron interaction between Pd and Cu (*SI Appendix*, Fig. S34). Intriguingly, the CV curve of $Pd_{67}Cu_{33}$ displayed a weak $^{-}$OH adsorption peak at 0.51 V, more negative than that of $Pd_{67}Ag_{33}$ (0.49 V), suggesting that the tensile strained lattice structure could contribute to enhancing the affinity of $^{-}$OH on catalyst and allowing the oxidation of $^{-}$OH into $*OH_{ad}$ at lower potential (*SI Appendix*, Fig. S35*A*). The EPR spectra and Fluorescence spectra also indicated the accelerated $*OH_{ad}$ productivity over the tensile strained $Pd_{67}Ag_{33}$ (*SI Appendix*, Fig. S35 *B* and *C*). The promotional effect of the lattice tensile strain is reflected by the lower mass activity of $Pd_{67}Cu_{33}$ with a lower $I_f/I_b$ value relative to those of $Pd_{67}Ag_{33}$, attributed to the significant role of $*OH_{ad}$ in boosting the conversion of intermediates and circumventing the poisoning effect (*SI Appendix*, Fig. S35*D*) (42, 43). Furthermore, the much lower onset potential of $Pd_{67}Ag_{33}$ in comparison to that of $Pd_{67}Cu_{33}$ further supported the accelerated EGOR kinetics by tensile strain effect (*SI Appendix*, Fig. S35*E*). Our investigation unveiled that the compressive strain on $Pd_{67}Cu_{33}$ resulted in the weakened adsorption of $^{-}$OH and hindered the subsequent activation process. This observation is aligned with previous studies suggesting the reduction in the binding strength of oxygen-containing intermediates on compressive strained catalysts (44). In summary, these findings affirmed that the tensile strain effect induced by Ag doping could signally improve the adsorption/activation behavior of $^{-}$OH on the catalyst, thereby optimizing the kinetics for EGOR.

To gain in-depth understanding of reaction mechanisms at the molecule level during the EG-to-GA conversion, electrochemical in situ FTIR spectroscopy was measured. In situ FTIR spectra were recorded within the potential range of 0 to 1.2 V (vs. RHE) at an interval of 100 mV in 1.0 M KOH and 1.0 M EG. The peak at 1,660 $cm^{-1}$ belongs to the 2-hydroxyacetyl ($*OC–CH_2OH$) intermediates, which were regarded as a key intermediate in the EG-to-GA conversion (26). The peak at 1,236 $cm^{-1}$ is assigned to C–O stretch of GA (45, 46). The bonds at 1,411 $cm^{-1}$ are responsible for symmetric stretch of $COO^{-}$ in GA. The peaks at 1,326 and 1,580 $cm^{-1}$ belong to the symmetric and antisymmetric stretching bands of $COO^{-}$ of GA, and the distinct vibration peak at 1,076 $cm^{-1}$ can be ascribed to the stretching vibration of aldehyde (–CHO) from glyoxal and GA species (18, 47). The bands at 1,307 and 1,340 $cm^{-1}$ are attributed to oxalate and carbonate ($CO_3^{2-}$) (46, 48). As depicted in Fig. 4 *E* and *F*, the bands at 1,076 and 1,580 $cm^{-1}$ appeared at 0.5 V vs. RHE on $Pd_{67}Ag_{33}$, lower than that of Pd (0.6 V vs. RHE), indicating that $Pd_{67}Ag_{33}$ exhibits a diminished energy barrier for the EG-to-GA conversion. Meanwhile, the comparison of in situ FTIR spectra between Pd and $Pd_{67}Ag_{33}$ revealed the significantly enhanced signals of GA (1,076, 1,236, 1,326, 1,411, and 1,580 $cm^{-1}$) on $Pd_{67}Ag_{33}$, while the intensity of bands associated with undesirable products (1,307 and 1,340 $cm^{-1}$) showed no noticeable change. This result further elucidated the improved GA selectivity on $Pd_{67}Ag_{33}$, aligning with the NMR results. In summary, the in situ FTIR spectra uncovered underlying reason why $Pd_{67}Ag_{33}$ could deliver excellent EGOR performance and GA selectivity, demonstrating that alloying Pd with other metals to modulate its electron and lattice structure is a promising strategy for enhancing the EG-to-GA conversion.

**DFT Calculations.** To elucidate the underlying factors responsible for the enhanced activity and GA selectivity originating from the ligand and strain effects triggered by Ag incorporation, DFT calculations were implemented. Specifically, we evaluated the adsorption energies of active species and intermediates on the model surfaces of Pd (111) and $Pd_{67}Ag_{33}$ (111) with 3.7% tensile strain (referred to as $Pd_{67}Ag_{33}$) (*SI Appendix*, Figs. S36–S40). Initially, the projected density of states (PDOS) analysis for the Pd d-band was calculated, revealing d-band center values of –1.65 eV for Pd (111) and –1.96 eV for $Pd_{67}Ag_{33}$ (111) (Fig. 5*A*), which were in good agreement with experimental measurements. The summarized adsorption energies in Fig. 5*B* demonstrate the weakened adsorption of $*OCCH_2OH$ intermediates and CO

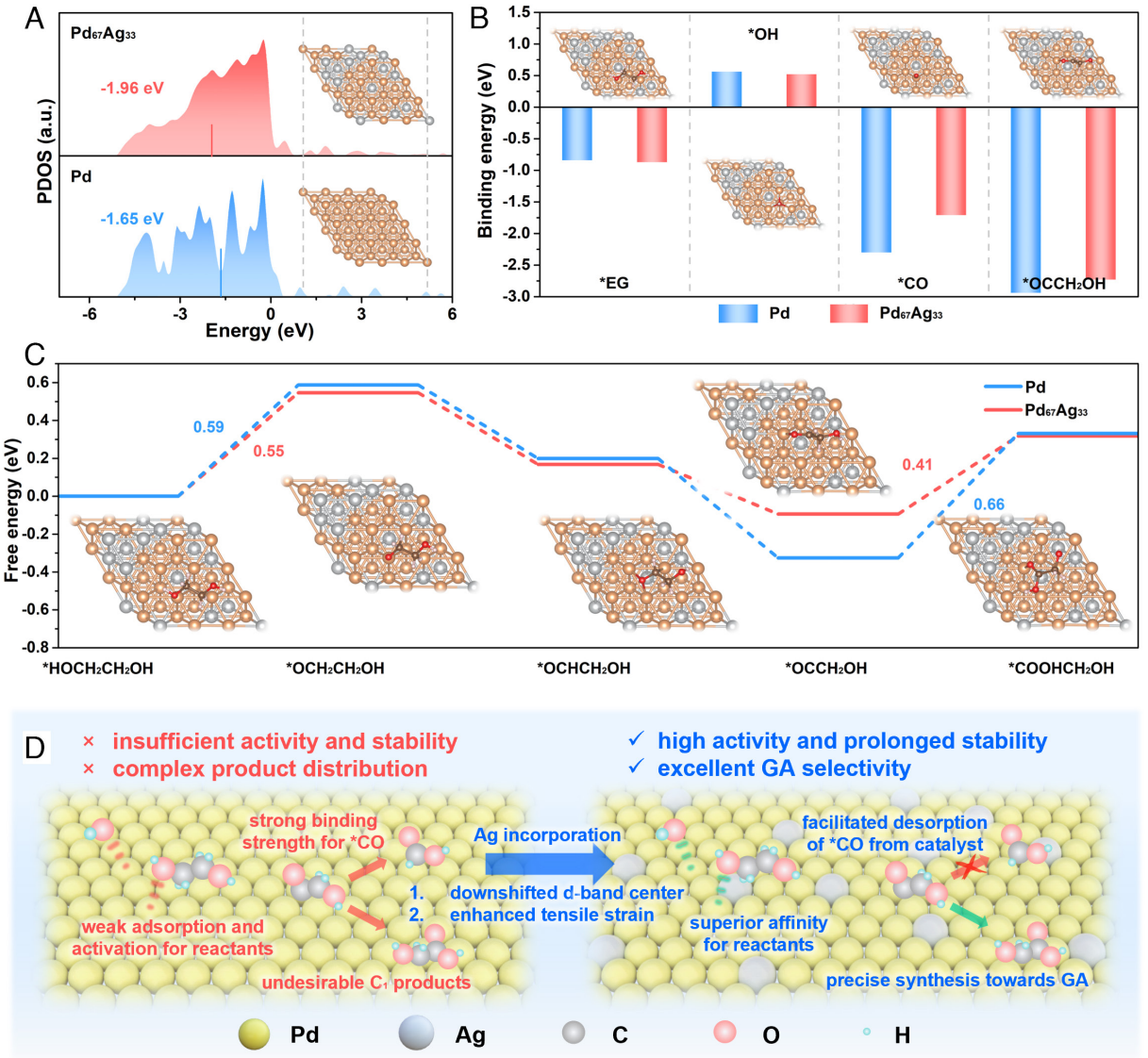


**Fig. 5.** DFT calculations. (*A*) PDOS (d-band center) of Pd and $Pd_{67}Ag_{33}$; the *Inset* shows the optimized configurations of Pd and $Pd_{67}Ag_{33}$. (*B*) Calculated adsorption energy of *EG, *OH, *CO, and *$OCCH_2OH$ on Pd (111) and $Pd_{67}Ag_{33}$ (111); the *Inset* shows the most energetically favorable adsorption configurations of molecules on $Pd_{67}Ag_{33}$. (*C*) Free-energy profile of the selective EGOR on $Pd_{67}Ag_{33}$ (111) and Pd (111). (*D*) Scheme of the proposed EGOR mechanism on Pd and $Pd_{67}Ag_{33}$.

on $Pd_{67}Ag_{33}$, which is in accordance with the previous studies that lowering the d-band center can weaken the adsorption of carbonyl species (12). Therefore, we confirmed that the facilitated release of *CO and *$OCCH_2OH$ are primarily attributed to the optimized electron structure (ligand effect), where the incorporation of Ag could effectively suppress excessive oxidation and poisoning allowing the high GA selectivity and stable long-term performance. Meanwhile, Fig. 5*B* illustrated the stronger adsorption of $^-$OH and EG on $Pd_{67}Ag_{33}$, which also aligns with the experimental observations. To further investigate the contribution of the strain effect, we discussed the adsorption of these key molecules on the model surface of $Pd_{67}Ag_{33}$ without tensile strain (referred to as $Pd_{67}Ag_{33}$-0%) (*SI Appendix*, Fig. S41). Notably, tensile strain plays a crucial role in enhancing the adsorption of EG and $^-$OH, thus boosting the activity for EGOR. Furthermore, we investigated the free energy diagrams of the involved intermediates during the selective EG-to-GA conversion on Pd (111) and $Pd_{67}Ag_{33}$ (111) (*SI Appendix*, Figs. S42 and S43). Fig. 5*C* demonstrated a lower energy barrier (0.55 eV) of H-abstraction on $Pd_{67}Ag_{33}$. Moreover, the *$OC–CH_2OH$ to *$COOH–CH_2OH$ conversion, regarded as a rate-determining step (RDS) in previous works, is facilitated by a reduced energy barrier on $Pd_{67}Ag_{33}$ (0.41 eV), indicating the rapid conversion toward the target GA product.

Based on the above experimental investigations and theoretical calculations, we proposed a mechanistic understanding of the electrochemical EG-to-GA conversion over $Pd_{67}Ag_{33}$ (Fig. 5*D*). First, the electron interaction between Pd and Ag atoms, known as ligand effect, decreased the d-band center of Pd, which weaken the binding strength of carbonyl species (e.g., *CO and *$OC–CH_2OH$) on catalyst. This feature effectively suppressed excessive oxidation and mitigated CO poisoning, thereby ensuring the C–C bond preserving pathway and superior long-term stability over the $Pd_{67}Ag_{33}$. Second, doping the Ag with larger atomic radius into Pd lattice introduced a 3.7% tensile strain in $Pd_{67}Ag_{33}$, which plays a vital role in strengthening the affinity toward reactants (e.g., EG and $^-$OH). Thus, $Pd_{67}Ag_{33}$ delivered the enhance catalytic activity for EGOR. As a contrast, the insufficient affinity for reactants and restrained desorption of carbonyl species on Pd should be responsible for the inferior activity and unsuppressed

$C_1$ products pathway. In summary, these findings collectively demonstrated that the synergy of the ligand effect and strain effect in PdAg alloy for the highly active and selective GA synthesis from PET wastes, which could provide guidance for the design of future catalysts for effective PET upcycling.

**Covalorization of PET-Derived EG and $CO_2$ in an Integrated Electrolyzer.** Electrochemical coupling of waste plastics valorization with $CO_2$ conversion provides a promising approach to upcycle waste carbon resources into valuable chemicals on both sides of the electrolyzer. Prior to the covalorization of PET and $CO_2$, we evaluated the electrochemical $CO_2$RR performance over $Pd_{67}Ag_{33}$ (*SI Appendix*, Figs. S44–S47), which delivered high current density of 10.8 mA $cm^{-2}$ at –0.35 V and a maximum FE of 92.5% for FA production at –0.27 V, consistent with the performance of previously reported Pd-based alloy electrocatalysts (23, 24, 49). The superior $CO_2$RR performance could be contributed to the ligand effect in $Pd_{67}Ag_{33}$, where electron interaction between Pd and Ag lowered the d-band center of Pd and thereby significantly enhanced its FA selectivity and CO tolerance. Consequently, the exceptional bifunctional properties of the $Pd_{67}Ag_{33}$ catalyst in electrochemical EGOR and $CO_2$RR hold great promise in developing a two-electrode integrated system. To this end, a two-electrode H-type electrolyzer was assembled by employing $Pd_{67}Ag_{33}$ catalysts on carbon paper as the anode and cathode. The anodic chamber contained 1 M KOH/1 M EG with $N_2$ gas flow, while the cathodic chamber was filled with 0.1 M $KHCO_3$ solution bubbled with $CO_2$, and two chambers were separated by a bipolar membrane (BPM) (*SI Appendix*, Fig. S48). Notably, this system first enables simultaneous anodic glycolate synthesis from PET-derived EG and cathodic $CO_2$-to-FA conversion, yielding attractive system-level performance. Specifically, the inclusion of EG leads to a significant reduction in overpotential of approximately 1,000 mV, at a current density of 2 mA $cm^{-2}$, indicative of the pronounced enhancement in cell performance achieved through the replacement of OER at the anode with EGOR (*SI Appendix*, Fig. S49). The chronoamperometric curve of the EGOR//$CO_2$RR integrated electrolyzer during electrolysis illustrated that $Pd_{67}Ag_{33}$ catalyst possesses good catalytic stability (*SI Appendix*, Fig. S50). In contrast to the EGOR//$CO_2$RR cell, bubble formation was observed on the surfaces of both electrodes in the OER//$CO_2$RR cell, with the cathodic bubbles primarily associated with the intensified side reaction of hydrogen evolution reaction (HER) under higher applied cell voltage (*SI Appendix*, Fig. S51). This finding suggests that a lowered applied potential can be achieved in the integrated cell as the substitution of OER with EGOR, which contributes to energy conservation and mitigates the undesired anodic HER.

$^1$H NMR spectrum of the electrolytes in each chamber revealed the product distribution, where GA and FA were identified as the primary products in the anodic and cathodic compartments, respectively (*SI Appendix*, Fig. S52). Quantitative analysis demonstrated that a maximum overall FE of approximately 163.5% for ideal carbonaceous products was achieved at a low cell voltage of 0.4 V, encompassing anodic $FE_{GA}$ of 81.7% and cathodic $FE_{FA}$ of 81.8% (*SI Appendix*, Fig. S53). This study provides compelling evidence for the successful production of separated FA and GA through the coelectrolysis of $CO_2$ and PET-derived EG over the bifunctional $Pd_{67}Ag_{33}$ catalyst. In comparison to previous studies that combined EGOR with cathodic HER (50, 51), the adoption of $CO_2$RR on cathode not only enables the utilization of carbonaceous resources for high-value chemicals production but also contributes to achieving carbon neutrality. However, it should be noted that the faradaic efficiency of cathodic FA production decreases as the cell voltage increases, primarily due to the intensified HER side reaction. To address this, future advancements in the rational design of cathodic $CO_2$RR catalysts to align with the working potential range of the anodic EGOR are expected to facilitate highly efficient co-upcycling of $CO_2$ and PET waste, opening a sustainable and economic path for the generation of value-added chemicals.

In conclusion, we designed a tensile strained $Pd_{67}Ag_{33}$ alloy aerogel as a highly active and selective catalyst for GA synthesis from waste PET plastics. The experiments and calculations demonstrated that the synergistic of tensile strained effect and the ligand effect of Ag doping affected the adsorption behaviors of reaction intermediates, thus contributing to the construction of the best active catalyst for EG-to-GA conversion observed thus far. Meanwhile, both the mass activity and GA selectivity of different $Pd_xAg_y$ catalysts displayed a volcanic trend along with the increasing of Ag fraction. This finding underscored the necessity, in the design of alloy catalysts for EG-to-GA conversion, to consider not only the ligand effect but also the strain effect, size effect, and mass transfer. The modulation of electron structure of Pd sites by Ag doping also allowed the superior cathodic $CO_2$RR performance on $Pd_{67}Ag_{33}$, which endow its promising as bifunctional catalyst for the covalorization of PET plastics and $CO_2$. Therefore, we first assembled an integrated electrolyzer for reforming PET and $CO_2$ into GA and FA, respectively, which demonstrates >80% FE on both electrodes for the desirable carbonaceous molecule at a low cell voltage of 0.4 V. Our findings not only provide insights into the synergistic of train effect and ligand effect in the enhancement of performance for EG-to-GA conversion over alloy catalyst, but also contribute to the construction of advanced covalorization system that achieves economic and sustainable utilization of carbon-rich wastes into high-value chemicals.

## Materials and Methods

**Chemicals.** Palladium chloride ($PdCl_2$) and silver nitrate ($AgNO_3$) were purchased from Aldrich Corp. Trisodium citrate dihydrate (NaCA) and potassium hydroxide (KOH) were purchased from Shanghai Aladdin Chemical Reagent Co. Ltd. $D_2O$ (for NMR, 99.9%) was purchased from Innochem Technology Co., Ltd. (Shanghai, China). All other reagents were purchased from Guoyao Chemical Company. All chemicals were of analytical grade and used without further purification. Deionized water (18 MΩ cm) was applied for all experiments.

**Pretreatment of Plastics.** 10 g of PET derived from waste plastic bottle was soaked in 100 mL 3 M KOH aqueous solution at 80 °C for 48 h with continuous stirring in a flask. The constituent unit (terephthalic acid, TPA) was separated from the solution hydrothermally treated via an acidification treatment using concentrated $H_2SO_4$. Residual EG was concentrated, purified, and solved in 1 M KOH for electrochemical upcycling.

**Synthesis of $Pd_xAg_y$ Aerogel.** Typically, the $Pd_{67}Ag_{33}$ aerogel was synthesized by a two-step strategy. First, 0.06 mmol $PdCl_2$, 0.12 mmol HCl, and 0.6 mmol NaCA were added into 300 mL of deionized water with stirring to form solution A. Next, 0.03 mmol $AgNO_3$ and 0.3 mmol NaCA were dissolved in 150 mL of deionized water to form solution B. Then, 1.2 and 0.6 mL freshly prepared $NaBH_4$ aqueous solution (200 mM) was rapidly injected into the solution A and solution B to form ligands stabilized Pd colloidal solution and Ag colloidal solution. After stirring for 90 s, the two colloidal solutions were uniformly mixed together. Subsequently, 4.5 mL aqueous solution containing 30 mmol $NH_4F$ was rapidly injected into the as-obtained mix solution. After continuous stirring for 180 s, $Pd_{67}Ag_{33}$ hydrogel was generated at the bottom of the glassware. To remove possible residues, the hydrogel was carefully washed with water for three times in 2 d. Afterward, the resulting hydrogel was flash-frozen by liquid nitrogen and dried by a freeze dryer. As such, other $Pd_xAg_y$ aerogels with various mole ratios were prepared by varying the mole ratios of Pd and Ag sources in the precursor solutions.

**Synthesis of $Pd_{67}Cu_{33}$ Aerogel.** $Pd_{67}Cu_{33}$ aerogel was synthesized using the similar two-step strategy by simply changing the species of metal precursors.

**Material Characterization.** TEM, high-resolution TEM (HRTEM) images, and elemental mapping analysis were performed on a Talos F200S. The aberration-corrected HAADF-STEM (AC- HAADF-STEM) and STEM-EDS were conducted on a Thermofisher Titan Themis Z. XRD patterns were conducted on a D8 Advance instrument (AXS-Bruker) with Cu Kα radiation. XPS measurement were done on an ESCALAB 250Xi. Elements and valence information were analyzed by the XPS peak software using setting to 20% Lorentzian and 80% Gaussian. The binding energy (B.E.) of all XPS data was calibrated vs. the standard $sp^2$ C 1 s peak at 284.6 eV. The d-band centers were calculated by following Eq. **1** (26). The surface morphologies were conducted by nitrogen sorption isotherms at 77 K on a Autosorb iQ instrument (Quantachrome), and the specific surface areas were calculated via a Brounauer–Emmett–Teller (BET) method. $^1$H NMR spectroscopy was measured on a 400 MHz/AVANCE NEO (Bruker). The *OH adspecies were detected by EPR (Bruker, Germany) with DMPO as capture agents.

$$\int_{-10\ \mathrm{eV}}^{0\ \mathrm{eV}(E_f)} (\text{binding energy (E)} \times \text{intensity (E) dE}) \Big/ \int_{-10\ \mathrm{eV}}^{0\ \mathrm{eV}(E_f)} \text{intensity (E) dE}. \quad [\mathbf{1}]$$

**Working Electrode Preparation.** The catalyst ink was prepared by ultrasonicating the suspension containing 1 mg of as-prepared catalyst, 400 isopropanol (IPA), 100 deionized water, and 2 μL of Nafion (5 wt.%) for 1 h. Then catalyst ink was dropped onto a L-type glassy-carbon electrode (GCE, 4 mm, ~0.1256 $cm^2$) and dried under ambient air. For the EGOR and $CO_2$RR half-reaction tests, the catalyst loading was 0.1 mg $cm^{-2}$ and 0.5 mg $cm^{-2}$, respectively. The working electrode for mass activity evaluation was prepared by using loading 2 μg catalyst onto GCE. For the long-term stability and H-cell tests, carbon paper (CP, 0.25 $cm^2$) with a catalyst loading of 0.5 mg $cm^{-2}$ served as the electrode.

**Electrochemical In Situ FTIR Reflection Spectroscopy.** To investigate the mechanism of EG-to-GA conversion at molecule level, in situ FTIR spectroscopy was collected by a Thermo 8700 spectrometer equipped with a liquid nitrogen-cooled mercury cadmium telluride detector (MCT-A). Electrochemical in situ FTIR spectra were carried out by utilizing a home-made thin-layer infrared (IR) cell with a three-electrode configuration, in which the electrolyte consists of 1 M potassium hydroxide (KOH) and 1 M ethylene glycol (EG). The as-synthesized electrocatalyst was used as the working electrode, while an Hg/HgO (1.0 M KOH) electrode and a platinum wire served as the reference and counterelectrodes, respectively. The FTIR spectra were collected over a potential range of 0 to 1.1 V (vs. RHE) at intervals of 0.1 V. During test, an incident IR beam was transmitted through a $CaF_2$ optical window and a thin-layer solution prior to being reflected off the electrode surface. The resulting spectra were recorded as the relative change in reflectivity and were calculated using the following equation:

$$\Delta R/R = (R(E_S) - R(E_R))/R(E_R), \quad [\mathbf{2}]$$

where $R(E_S)$ and $R(E_R)$ are the single-beam spectra obtained at the catalyst potential ($E_S$) and reference potential ($E_R$), respectively.

**Electrochemical Measurements.** Electrochemical EGOR measurements were equipped with a standard three-electrode single cell at room temperature with a working electrode, a platinum counterelectrode (1 $cm^2$), and an Hg/HgO (1.0 M KOH) reference electrode. An electrolyte solution containing 1 M EG and 1 M KOH was used for all EGOR tests. As for the electrochemical measurements, the electrolyte was bubbled with $N_2$ (99.99%) for ~30 min to ensure $N_2$ saturation during tests. Chronoamperometric curves were collected at the potentials between 0.6 and 1.1 V. LSV curves were recorded at 10 mV/s unless special situation. EIS results were performed over a frequency range from 0.01 Hz to 100 kHz with a perturbation of 5 mV. A custom-made three-electrode system was used to investigate the electrochemical $CO_2$RR in H-cell, where a platinum electrode (1 $cm^2$) and Ag/AgCl electrode (4.0 M KCl) served as the counterelectrode and reference electrode. The two chambers contained 15 mL of 0.1 M $KHCO_3$ aqueous solution (pH = 8.2) and were separated by a cation exchange membrane (Nafion 117). Before tests, the cathodic electrolyte was purged with $CO_2$ for 30 min at a constant rate of 20 sccm to maintain its saturation (pH = 6.8) during measurements. Chronoamperometric curves were collected at the potentials between −0.35 and 0 V (vs. RHE).

All electrochemical measurements were connected to an electrochemical workstation (VMP3, Bio-logic, France). All potentials were calibrated to the RHE based on the following equation:

$$E_{RHE} = E_{Hg/HgO} + 0.098 + 0.059\ \mathrm{pH}, \quad [\mathbf{3}]$$

$$E_{RHE} = E_{Ag/AgCl} + 0.2046 + 0.059\ \mathrm{pH}. \quad [\mathbf{4}]$$

For the EGOR//$CO_2$RR two-electrode system, the electrochemical measurements were carried out in an H-type cell with a BPM to separate the two chambers.

**Product Analysis.** The NMR samples contained 500 μL of electrolyte, 100 mL of $D_2O$, and 100 μL of dimethyl sulfoxide (DMSO) water solution (1% Vol.). The presaturation method was used to suppress the water peak.

The FE (%) of the GA formation can be determined by the following Eq. **5**, n is the number of exchanged electrons to produce the final products (i.e., GA and FA):

$$\mathrm{FE}(\%) = \frac{n \times \text{obtained product (mol)} \times 96{,}485\ (\mathrm{C/mol})}{\text{Total charge passed (C)}} \times 100\%, \quad [\mathbf{5}]$$

where n is the number of electron transfer for each product formation, n = 2 for FA, n = 4 for GA; 96,485 C $mol^{-1}$ is the Faraday constant.

**Computational Methods.** First-principles calculations based on spin-polarization DFT have been conducted using the generalized gradient approximation (GGA) with the Perdew–Burke–Ernzerhof (PBE) formulation (52–54). The ionic cores have been described using projected augmented wave (PAW) potentials (55, 56), while the valence electrons have been treated within a plane wave basis set with a kinetic energy cutoff of 450 eV. Van der Waals interactions have been accounted for using the DFT-D3 method proposed by Grimme (57, 58). The electronic energy convergence criterion was set at $10^{-5}$ eV, indicating self-consistency. Geometry optimization was considered converged when the energy change was below 0.02 eV $Å^{-1}$. A 2 × 2 × 1 gamma-centered grid was employed for Brillouin zone sampling during relaxation, and a 15 Å vacuum layer was added to eliminate spurious interactions between periodic images. Spin-polarized calculations were performed to obtain the desired results. The adsorption energy ($E_{ads}$) is calculated as

$$E_{ads} = E_{total} - E_{slab} - E_{adsorbate}, \quad [\mathbf{6}]$$

where the $E_{total}$ is the total energy of an optimized slab with the adsorbate on it, $E_{slab}$ is the energy of a relaxed clean slab, and $E_{adsorbate}$ is the energy of an adsorbate molecule.

The Gibbs free energy diagram (ΔG) of the EGOR was determined using the computational hydrogen electrode (CHE) model proposed (59). In this model, the free energy of the proton-electron pair was equated to that of 1/2 $H_2$(g). The free energy change for each step was computed by

$$\Delta G = \Delta E + \Delta ZPE - \Delta TS, \quad [\mathbf{7}]$$

where ΔE was the energy difference of the reactants and the products directly obtained from DFT calculation. ΔZPE is the contribution of variation of zero-point energy (ZPE), ΔS is the entropy (S) change, T is the temperature (T = 298.15 K).

It is imperative to underscore that while we employed the most commonly proposed mechanism along as well as well-defined and widely accepted models, constructing computational models becomes notably challenging in multimetallic alloys with complex contents. Meanwhile, the inclusion of additional factors into the model may introduce potential influences on the computational results (60).

**Data, Materials, and Software Availability.** All study data are included in the article and/or *SI Appendix*.

**ACKNOWLEDGMENTS.** We acknowledge the financial support by the National Key R&D Program of China (2022YFA1503501), Shanghai Committee of Science and Technology, China (No. 21ZR1480000), the National Natural Science Foundation of China (Nos. 52122312 and U21A20329), Shanghai International

Science and Technology Partnership Project (23520750400), the Fundamental Research Funds for the Central Universities and Graduate Student Innovation Fund of Donghua University (CUSF-DH-D-2022001), State Key Laboratory for Modification of Chemical Fibers and Polymer Materials, Donghua University.

Author affiliations: [a]State Key Laboratory for Modification of Chemical Fibers and Polymer Materials, College of Materials Science and Engineering, Donghua University, Shanghai 201620, China; and [b]Department of Chemistry, Shanghai Key Laboratory of Molecular Catalysis and Innovative Materials and State Key Laboratory of Molecular Engineering of Polymers, Fudan University, Shanghai 200433, China

1. R. Geyer, J. R. Jambeck, K. L. Law, Production, use, and fate of all plastics ever made. *Sci. Adv.* **3**, e1700782 (2017).
2. C. C. Chen *et al.*, General features to enhance enzymatic activity of poly(ethylene terephthalate) hydrolysis. *Nat. Catal.* **4**, 425–430 (2021).
3. J. L. Chen *et al.*, How to build a microplastics-free environment: strategies for microplastics degradation and plastics recycling. *Adv. Sci.* **9**, 2103764 (2022).
4. Y. Li *et al.*, Catalytic transformation of PET and $CO_2$ into high-value chemicals. *Angew. Chem. Int. Ed.* **61**, e202117205 (2022).
5. Y. Jing *et al.*, Towards the circular economy: Converting aromatic plastic waste back to arenes over a $Ru/Nb_2O_5$ catalyst. *Angew. Chem. Int. Ed.* **60**, 5527–5535 (2021).
6. N. A. Rorrer *et al.*, Combining reclaimed PET with bio-based monomers enables plastics upcycling. *Joule* **3**, 1006–1027 (2019).
7. Y. Liu *et al.*, Photothermal catalytic polyester upcycling over cobalt single-site catalyst. *Adv. Funct. Mater.* **33**, 2210283 (2022).
8. Y. Liu *et al.*, Solar thermal catalysis for sustainable and efficient polyester upcycling. *Matter* **5**, 1305–1317 (2022).
9. H. Lu *et al.*, Machine learning-aided engineering of hydrolases for PET depolymerization. *Nature* **604**, 662–667 (2022).
10. J. L. Chen *et al.*, Toward carbon neutrality: Selective conversion of waste plastics into value-added chemicals. *Matter* **6**, 3322–3347 (2023).
11. Q. Mao *et al.*, In situ reconstruction of partially hydroxylated porous Rh metallene for ethylene glycol–assisted seawater splitting. *Adv. Funct. Mater.* **32**, 2201081 (2022).
12. F. Liu *et al.*, Concerted and selective electrooxidation of polyethylene-terephthalate-derived alcohol to glycolic acid at an industry-level current density over a $Pd-Ni(OH)_2$ catalyst. *Angew. Chem. Int. Ed.* **62**, e202300094 (2023).
13. Y. Yan *et al.*, Electrocatalytic upcycling of biomass and plastic wastes to biodegradable polymer monomers and hydrogen fuel at high current densities. *J. Am. Chem. Soc.* **145**, 6144–6155 (2023).
14. F. Gao, Y. Zhang, F. Ren, Y. Shiraishi, Y. Du, Universal surfactant-free strategy for self-standing 3D tremella-like Pd–M (M = Ag, Pb, and Au) nanosheets for superior alcohols electrocatalysis. *Adv. Funct. Mater.* **30**, 2000255 (2020).
15. J. Lai *et al.*, Efficient bifunctional polyalcohol oxidation and oxygen reduction electrocatalysts enabled by ultrathin PtPdM (M = Ni, Fe, Co) nanosheets. *Adv. Energy Mater.* **9**, 1800684 (2019).
16. Y. Zhu *et al.*, Single-atom in-doped subnanometer Pt nanowires for simultaneous hydrogen generation and biomass upgrading. *Adv. Funct. Mater.* **30**, 2004310 (2020).
17. X. Yang *et al.*, Modulating electronic structure of an Au-nanorod-core–PdPt-alloy-shell catalyst for efficient alcohol electro-oxidation. *Adv. Energy Mater.* **11**, 2100812 (2021).
18. Y. Qin *et al.*, Extraordinary p-d hybridization interaction in heterostructural Pd-PdSe nanosheets boosts C–C bond cleavage of ethylene glycol electrooxidation. *Angew. Chem. Int. Ed.* **61**, e202200899 (2022).
19. M. Luo *et al.*, PdMo bimetallene for oxygen reduction catalysis. *Nature* **574**, 81–85 (2019).
20. Y. Zhang *et al.*, Rhombohedral Pd-Sb nanoplates with Pd-terminated surface: An efficient bifunctional fuel-cell catalyst. *Adv. Mater.* **34**, 2202333 (2022).
21. J. A. Zamora Zeledon *et al.*, Tuning the electronic structure of Ag-Pd alloys to enhance performance for alkaline oxygen reduction. *Nat. Commun.* **12**, 620 (2021).
22. R. Du *et al.*, Unveiling reductant chemistry in fabricating noble metal aerogels for superior oxygen evolution and ethanol oxidation. *Nat. Commun.* **11**, 1590 (2020).
23. Y. Zhou *et al.*, Mesoporous PdAg nanospheres for stable electrochemical $CO_2$ reduction to formate. *Adv. Mater.* **32**, 2000992 (2020).
24. N. Han *et al.*, Alloyed palladium-silver nanowires enabling ultrastable carbon dioxide reduction to formate. *Adv. Mater.* **33**, 2005821 (2021).
25. S. Zhang *et al.*, Highly strained Au-Ag-Pd alloy nanowires for boosted electrooxidation of biomass-derived alcohols. *Nano Lett.* **21**, 1074–1082 (2021).
26. D. Si, B. Xiong, L. Chen, J. Shi, Highly selective and efficient electrocatalytic synthesis of glycolic acid in coupling with hydrogen evolution. *Chem. Catal.* **1**, 941–955 (2021).
27. Y. Zhao *et al.*, Surface reconstruction of ultrathin palladium nanosheets during electrocatalytic $CO_2$ reduction. *Angew. Chem. Int. Ed.* **59**, 21493–21498 (2020).
28. F. Lv *et al.*, Au clusters on Pd nanosheets selectively switch the pathway of ethanol electrooxidation: Amorphous/crystalline interface matters. *Adv. Energy Mater.* **11**, 2100187 (2021).
29. J. Zhang *et al.*, Cr-doped Pd metallene endows a practical formaldehyde sensor new limit and high selectivity. *Adv. Mater.* **34**, 2105276 (2022).
30. B. Jiang *et al.*, Noble-metal–metalloid alloy architectures: Mesoporous amorphous iridium-tellurium alloy for electrochemical $N_2$ reduction. *J. Am. Chem. Soc.* **145**, 6079–6086 (2023).
31. Y. Kang *et al.*, Soft template-based synthesis of mesoporous phosphorus- and boron-codoped NiFe-based alloys for efficient oxygen evolution reaction. *Small* **18**, 2203411 (2022).
32. R. Liu *et al.*, Atomic-level-designed catalytically active palladium atoms on ultrathin gold nanowires. *Adv. Mater.* **29**, 1604571 (2016).
33. D. Zhou *et al.*, NiFe hydroxide lattice tensile strain: Enhancement of adsorption of oxygenated intermediates for efficient water oxidation catalysis. *Angew. Chem. Int. Ed.* **58**, 736–740 (2019).
34. C. Li, S. Yan, J. Fang, Construction of lattice strain in bimetallic nanostructures and its effectiveness in electrochemical applications. *Small* **17**, 2102244 (2021).
35. E. A. Moges *et al.*, Sustainable synthesis of dual single-atom catalyst of $Pd-N_4/Cu-N_4$ for partial oxidation of ethylene glycol. *Adv. Funct. Mater.* **32**, 2206887 (2022).
36. M. Du *et al.*, Electrochemical production of glycolate fuelled by polyethylene terephthalate plastics with improved techno-economics. *Small* **19**, 2303693 (2023).
37. L. Karuppasamy, C. Y. Chen, S. Anandan, J. J. Wu, Low- and high-index faceted pd nanocrystals embedded in various oxygen-deficient $WO_x$ nanostructures for electrocatalytic oxidation of alcohol (EOA) and carbon monoxide (CO). *ACS Appl. Mater. Interfaces* **11**, 10028–10041 (2019).
38. M. Zhou *et al.*, Synthesis of $Pd_3Sn$ and PdCuSn nanorods with $L1_2$ phase for highly efficient electrocatalytic ethanol oxidation. *Adv. Mater.* **34**, 2106115 (2022).
39. L. Luo *et al.*, Selective photoelectrocatalytic glycerol oxidation to dihydroxyacetone via enhanced middle hydroxyl adsorption over a $Bi_2O_3$-incorporated catalyst. *J. Am. Chem. Soc.* **144**, 7720–7730 (2022).
40. C. Li *et al.*, Dendritic defect-rich palladium-copper-cobalt nanoalloys as robust multifunctional non-platinum electrocatalysts for fuel cells. *Nat. Commun.* **9**, 3702 (2018).
41. H. Lv, L. Sun, Y. Wang, S. Liu, B. Liu, Highly curved, quasi-single-crystalline mesoporous metal nanoplates promote C-C bond cleavage in ethanol oxidation electrocatalysis. *Adv. Mater.* **34**, 2203612 (2022).
42. J. Zhu *et al.*, Ultrahigh stable methanol oxidation enabled by a high hydroxyl concentration on Pt clusters/MXene interfaces. *J. Am. Chem. Soc.* **144**, 15529–15538 (2022).
43. Y. Li *et al.*, The decisive role of adsorbed OH* in low-potential CO electro-oxidation on single-atom catalytic sites. *Carbon Energy* **5**, e310 (2023).
44. M. Li *et al.*, Exclusive strain effect boosts overall water splitting in PdCu/Ir core/shell nanocrystals. *Angew. Chem. Int. Ed.* **60**, 8243–8250 (2021).
45. H. Wang *et al.*, Electrocatalysis of ethylene glycol oxidation on bare and bi-modified Pd concave nanocubes in alkaline solution: An interfacial infrared spectroscopic investigation. *ACS Catal.* **7**, 2033–2041 (2017).
46. J.-X. Tang *et al.*, Screw-like PdPt nanowires as highly efficient electrocatalysts for methanol and ethylene glycol oxidation. *J. Mater. Chem. A* **6**, 2327–2336 (2018).
47. X.-Y. Ma *et al.*, The electrocatalytic activity and selectivity of ethylene glycol oxidation into value-added chemicals at iron-group electrodes in alkaline media. *Mater. Today Phys.* **37**, 101191 (2023).
48. X. Yang *et al.*, Interface-rich three-dimensional Au-doped PtBi intermetallics as highly effective anode catalysts for application in alkaline ethylene glycol fuel cells. *Adv. Funct. Mater.* **31**, 2103671 (2021).
49. R. Zhou *et al.*, Two-dimensional palladium-copper alloy nanodendrites for highly stable and selective electrochemical formate production. *Nano Lett.* **21**, 4092–4098 (2021).
50. F. Liu, X. Gao, R. Shi, E. C. M. Tse, Y. Chen, A general electrochemical strategy for upcycling polyester plastics into added-value chemicals by a $CuCo_2O_4$ catalyst. *Green Chem.* **24**, 6571–6577 (2022).
51. H. Zhou *et al.*, Electrocatalytic upcycling of polyethylene terephthalate to commodity chemicals and $H_2$ fuel. *Nat. Commun.* **12**, 4679 (2021).
52. G. Kresse, J. Furthmüller, Efficiency of ab-initio total energy calculations for metals and semiconductors using a plane-wave basis set. *Comput. Mater. Sci.* **6**, 15–50 (1996).
53. G. Kresse, J. Furthmuller, Efficient iterative schemes for ab initio total-energy calculations using a plane-wave basis set. *Phys. Rev. B* **54**, 11169–11186 (1996).
54. J. P. Perdew, K. Burke, M. Ernzerhof, Generalized gradient approximation made simple. *Phys. Rev. Lett.* **77**, 3865–3868 (1996).
55. P. E. Blochl, Projector augmented-wave method. *Phys. Rev. B* **50**, 17953–17979 (1994).
56. G. Kresse, D. Joubert, From ultrasoft pseudopotentials to the projector augmented-wave method. *Phys. Rev. B* **59**, 1758–1775 (1999).
57. S. Grimme, J. Antony, S. Ehrlich, H. Krieg, A consistent and accurate ab initio parametrization of density functional dispersion correction (DFT-D) for the 94 elements H-Pu. *J. Chem. Phys.* **132**, 154104 (2010).
58. S. Grimme, S. Ehrlich, L. Goerigk, Effect of the damping function in dispersion corrected density functional theory. *J. Comput. Chem.* **32**, 1456–1465 (2011).
59. J. K. Nørskov *et al.*, Origin of the overpotential for oxygen reduction at a fuel-cell cathode. *J. Chem. Phys. B* **108**, 17886–17892 (2004).
60. Y. Kang *et al.*, Mesoporous multimetallic nanospheres with exposed highly entropic alloy sites. *Nat. Commun.* **14**, 4182 (2023).